ADVANCED MATERIALS TECHNOLOGIES
www.advmattechnol.de

Post-Processing Strengthened 3D Artificial Fingertip with Multi-Intensity Pain Perception

Huijing Li, Felix Thasan, Tongtong Cui, Raihan Alfaridzi, Andreas Stihl, Felix H. Schacher, and Patrick Théato**

Artificial electric skin with multi-intensity pain-evaluating capabilities offers promising opportunities for the construction of friendly human-robot interaction. However, realizing a stepwise sensing system generally requires lateral integration of diverse materials, which is prone to delamination and thus operation failure. Here, a fully soft, monolithic hydrogel-based artificial fingertip (HBAF), fabricated via digital light processing (DLP) 3D printing, enabling robotic fingertips to distinguish objects in varying sizes is proposed. To enhance the mechanical and conductive properties of a printed hydrogel, a two-step post-processing method is developed to introduce a secondary functional network into a high-resolution soft model. This modification can increase stretchability by three-fold and conductivity by 1.78-fold compared to the original printed hydrogel. Notably, the integration challenge between the hydrogel-based sensor and the robotic body part is addressed by growing a polydopamine gel layer at the interface of the 3D model's base to enhance contact. Furthermore, the HBAF's size parameters can be programmed to achieve distinct pain thresholds, demonstrating its potential for personalized bionic sensors in artificial limbs and enhancing safety in collaborative robotics.

1. Introduction

The human hand is one of the most essential organs for interacting with our environment and performing daily activities, such as playing the piano, writing, or gripping objects. The hairless skin of the hand contains a high density of tactile afferents, which generate distinct neural impulses upon object interaction, enabling the evaluation of physical properties and contact dynamics.[1–4] Individuals with impaired tactile sensitivity struggle with these tasks due to insufficient mechanical feedback, hindering the brain's ability to plan and control object manipulation. Inspired by human biomechanics, humanoid robotics and prosthetic limbs aim to replicate similar movements or assist in daily tasks. However, robotic hands face significant challenges in grasping delicate or deformable objects, as they lack the soft, compliant structure of human skin and muscle.[5] While visual feedback provides indirect information about interactions, proprioception alone offers limited sensitivity to fingertip-level mechanical events. Thus, integrating a suitable tactile sensing system into robotic fingertips is critical for closed-loop control. Among key tactile cues, pain perception plays a vital role in self-protection by triggering avoidance behaviors and regulating contact forces.[6] For prosthetic users, an artificial hand with pain-like feedback could enhance both functional utility and psychological

H. Li, F. Thasan, T. Cui, P. Théato
Institute for Chemical Technology and Polymer Chemistry (ITCP)
Karlsruhe Institute of Technology (KIT)
Engesserstraße 18, D-76131 Karlsruhe, Germany
E-mail: hui.li@kit.edu; patrick.theato@kit.edu

P. Théato
Soft Matter Synthesis Laboratory
Institute for Biological Interfaces III
Karlsruhe Institute of Technology (KIT)
Hermann-von-Helmholtz-Platz 1, D-76344 Eggenstein-Leopoldshafen, Germany

The ORCID identification number(s) for the author(s) of this article can be found under https://doi.org/10.1002/admt.202501896

DOI: 10.1002/admt.202501896

R. Alfaridzi
RPTU Kaiserslautern-Landau
Gottlieb-Daimler-Straße, D-67663 Kaiserslautern, Germany

A. Stihl, F. H. Schacher
Institute of Organic Chemistry and Macromolecular Chemistry (IOMC)
Friedrich Schiller University Jena (FSU)
Lessingstraße 8, D-07743 Jena, Germany

A. Stihl, F. H. Schacher
Jena Center for Soft Matter (JCSM)
Friedrich-Schiller-University Jena
Philosophenweg 7, D-07743 Jena, Germany

F. H. Schacher
Helmholtz Institute for Polymers in Energy Applications Jena (HIPOLE Jena)
Lessingstraße 12-14, 07743 Jena, Germany

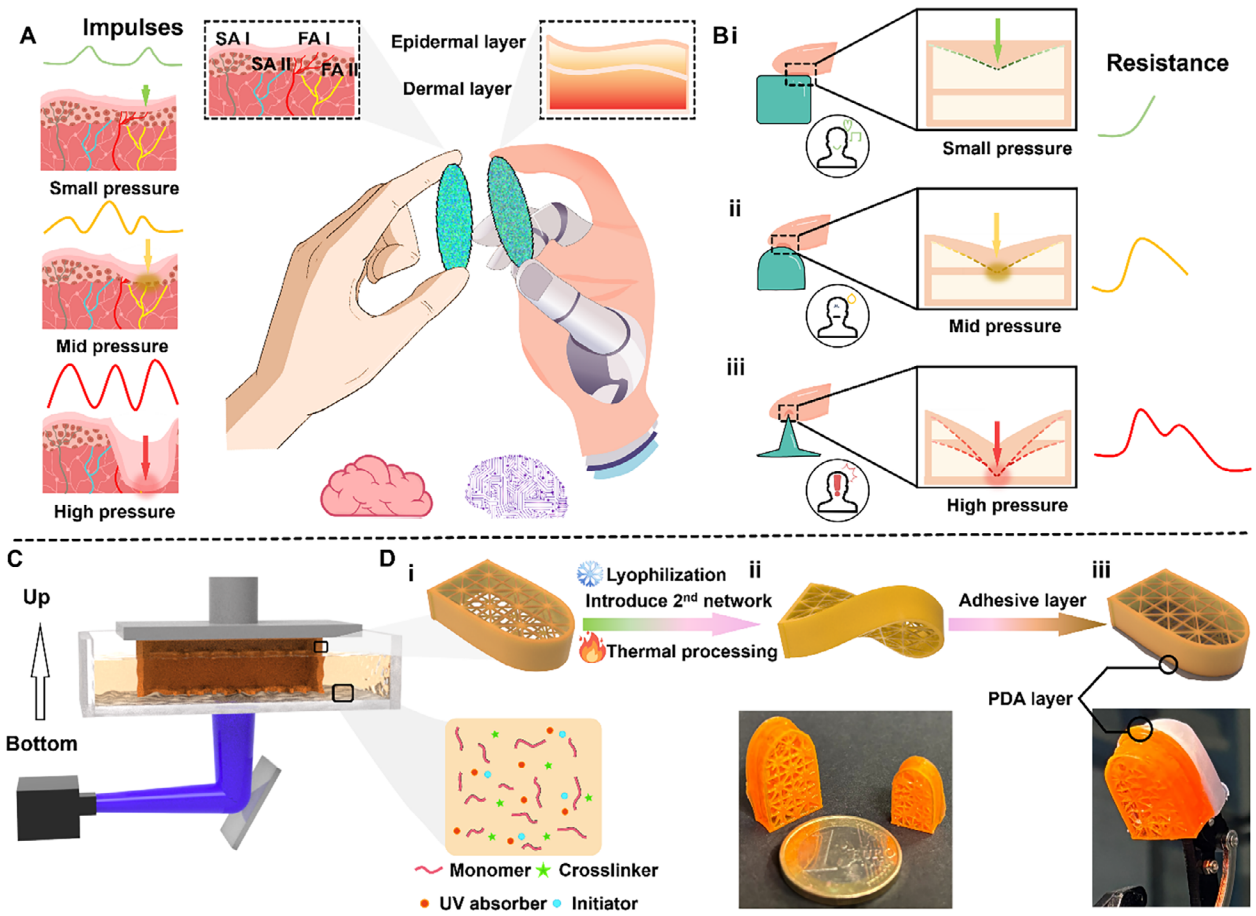

Figure 1. Schematic diagram of a hydrogel-based artificial fingertip (HBAF). A) Human skin contains mechanoreceptors distributed across epidermal and dermal layers that exhibit graded activation under increasing mechanical stimuli. B) Mimicking the three-layer architecture of human skin, the HBAF incorporates a stratified sensing structure. Upon contact with objects of varying radius, interlayer short-circuiting occurs through overlapping conductive pathways. This enables two orders of pain classification based on signal burst. C) The monolithic HBAF is fabricated via digital light processing (DLP) printing, which photopolymerizes monomeric ink into precise hydrogel structures while maintaining structural integrity. D) After two-step post-processing i), the relative hard gel model becomes stretchable ii). iii) A polydopamine (PDA) adhesive layer is subsequently grown at the base to facilitate robust robotic integration.

embodiment, bridging the gap between synthetic and biological limbs.

Recent approaches to mimicking pain perception can be categorized into two primary strategies: threshold control[6–13] and multi-channel monitoring.[5] In threshold control systems, a predefined "pain threshold" is established. When sensor signals (e.g., resistance,[6–8,10,11] capacitance[9,12]) exceed this threshold, the control system interprets them as pain and initiates appropriate responses. Yu et al.[9] implemented this concept using a delayered E-skin with transistor-based circuitry, where transistor activation was governed by the magnitude of the current. While this threshold-based control system offers straightforward implementation, its binary (on/off) operational modality significantly limits functional versatility in pain response modulation. Zhou et al.[6] advanced this approach by developing a suspended layered structure with closed-loop control, achieving enhanced tactile sensing accuracy and diverse programmable responses. However, this system compromises flexibility and softness due to its rigid plastic frameworks. Additionally, the material mismatch between rigid structural components and soft sensing layers introduces potential delamination risks under mechanical loading. Alternatively, multi-channel monitoring systems more closely replicate the biological organization of human glabrous skin. The human hand integrates four functionally distinct tactile afferent types: FA-I (fast-adapting type I) and SA-I (slow-adapting type I) receptors terminate superficially in the epidermal layer, responding to sustained deformation, while FA-II and SA-II receptors located deeper in the dermis detect low-frequency vibrations and static forces (**Figure 1A**).[14,15] These receptors generate characteristic impulse patterns in response to mechanical stimuli. Inspired by this architecture, Osborn et al.[5] developed an overlapping piezoresistive sensor array where high-pressure stimuli activate deeper embedded sensor layers, enabling simultaneous multi-channel signal analysis. While biologically plausible, this approach presents significant challenges in data processing complexity and structural integrity maintenance due to its multilayer configuration.

A stepwise sensing mechanism is crucial for accurate pain perception in artificial tactile systems. While human skin achieves stable, multi-threshold sensing with its multi-layer structure,

conventional artificial approaches relying on multi-material integration face challenges in structural stability and fabrication complexity. Here, we developed a monolithic hydrogel-based artificial fingertip (HBAF) with integrated multi-intensity pain perception, featuring a stable 3D three-layer structure (Figure 1A). The HBAF exhibits graded nociceptive responses: under the same gripping force, when contacting a flat surface, a relative low pressure only activates the first layer, producing an increasing resistance signal (Figure 1Bi). Under concentrated pressure from sharper objects (smaller radius at constant force), subsequent layer contacts trigger abrupt resistance drops corresponding to distinct pain intensities (Figure 1Bii). Such a multi-threshold response enables quantitative danger assessment, showing great potential to allow robotic systems to dynamically adjust interactions based on stimulus.

Achieving accurate pressure-dependent sensing requires precise control of the HBAF's mechanical properties, which translates into challenges in fabrication. During the digital light processing (DLP), the photocurable resin should be rapidly cured (<30 s), resulting in relatively high stiffness to prevent vertical deformation during the bottom-up printing process (Figure 1C).[16–19] Consequently, while as-printed 3D structures exhibit high spatial resolution (Figure 1Di), they typically demonstrate limited stretchability. To address this limitation, we developed a two-step post-processing method comprising freeze-drying followed by thermal annealing. This approach introduces a secondary elastomeric network within a 3D printed hydrogel matrix (Figure 1D ii), enhancing stretchability while preserving structural fidelity. Another critical challenge emerged during system integration: the hydrophilic HBAF's incompatibility with conventional hydrophobic robotic components (metallic/ plastic interface). We addressed this interfacial mismatch by growing a bioinspired polydopamine (PDA) adhesive layer[20] at the HBAF's base through in situ polymerization. The soft adhesive layer shows a huge possibility for combining HBAF on various robotic components with uneven surfaces. This fabrication of a fully soft stepwise pain sensor is highly programmable in terms of the pain threshold and safe factor, shows great promise in building a friendly human-robotic interface, and robotics with a humanoid reacting system.

2. Result and Discussion

2.1. Fabrication and Mechanical Properties

The two-step post-processing method for the hydrogel in HBAF is summarized in **Figure 2A**. Here, the hydrogel ink consists of acrylic acid (AAc) as the monomer, with sodium hydroxide (NaOH) added to saturate the free acrylic acid anions and suppress swelling of the printed layer during DLP printing. *N,N'*-Methylenebisacrylamide (Bis) serves as the chemical crosslinker (Figure 2Ai). A water-soluble derivative of 2,4,6-trimethylbenzoyl-diphenylphosphine oxide (TPO) was prepared and used as the initiator (TPO-Li) (Figure S1, Supporting Information).[21–23] To determine optimal printing conditions, we employed *Jacob's* working curve analysis.[24–26] This established DLP characterization method plots curing energy against cure depth on semi-log axes, revealing the ink's photopolymerization behavior at varying light intensities. The model's derivation assumes *Beer–Lambert* light absorption and is mathematically described by:

$$C_d = D_p \ln\left(\frac{E}{E_c}\right) \tag{1}$$

where C_d is the depth of cure at a given exposure intensity E, D_p is the penetration depth of the ink at the given wavelength (365 nm), and E_c is the critical exposure to start the polymerization or gelation. The measured curing depth as a function of exposure energy showed excellent correlation with the working curve model (Figure 2B), demonstrating the ink's effective curing characteristics. The printed hydrogel (G-PAAc) featured a high resolution (Figure S2, Supporting Information). To introduce the second functional network, the G-PAAc was first lyophilized to obtain a freeze-dried foam. Then the amphiphilic polymeric network, poly[(2-methacryloyloxy)ethyl trimethylammonium chloride] (PMETAC), formed inside the hydrogel after swelling and UV curing. Energy-dispersive X-ray (EDX) spectroscopy was employed to analyze and spatially resolve nitrogen distribution patterns in the hydrogel samples both before and after PMETAC incorporation (Figure S3, Supporting Information). The obtained results confirmed that the nitrogen content increased significantly after UV curing, indicative for a successful PMETAC network formation. As shown in the SEM-EDX mapping image (Figure 2Ci), the N atoms from PMETAC are homogeneously dispersed inside the hydrogel, indicating that the PMETAC network is formed evenly throughout the sample. As shown in Figure 2Aii, the hydrophobic polyester clusters (yellow regions) formed within the hydrated hydrogel matrix, which can be clearly distinguished by scattered shadows in the atomic force microscopy (AFM) phase image (Figure 2Cii) of a hydrogel sample and transmission electron microscopy (TEM) image from a dried sample (Figure S4, Supporting Information). Furthermore, differential scanning calorimetry (DSC) studies (Figure S5, Supporting Information) eliminated the existence of crystallization in the resulting hydrogel samples.

To further regulate the mechanical and conductive properties of the resulting hydrogel, thermal annealing processing was conducted according to the specific surface area, the detailed definition can be seen in Supporting Information. Under the same annealing temperature, the amount of water evaporation is proportional to the specific surface area of the model. Thus, to keep the evaporated water volume constant, the annealing time (T) must be proportional to the specific surface area (SSA),

$$T = SSA \times T_{unit} \tag{2}$$

where T refers to the annealing time with unit of minute (min), SSA means the specific surface area of the model with unit of m^{-1}, T_{unit} means unit annealing time with unit of min•m. Here, the unit annealing time is 5.21, 10.42, 15.63, and 20.84 min•m , with corresponding annealing temperature being 60 °C (Table S1, Supporting Information). The hydrogel samples are named G-0, G-5.21, G-10.42, G-15.63, and G-20.84, respectively. With decreasing water content (Figure 2D), the polymeric network became denser. Thus, the mechanical strength of the hydrogel and its water content are typically inversely correlated.[27] As seen in Figure 2E, the toughness increased with longer heating time.

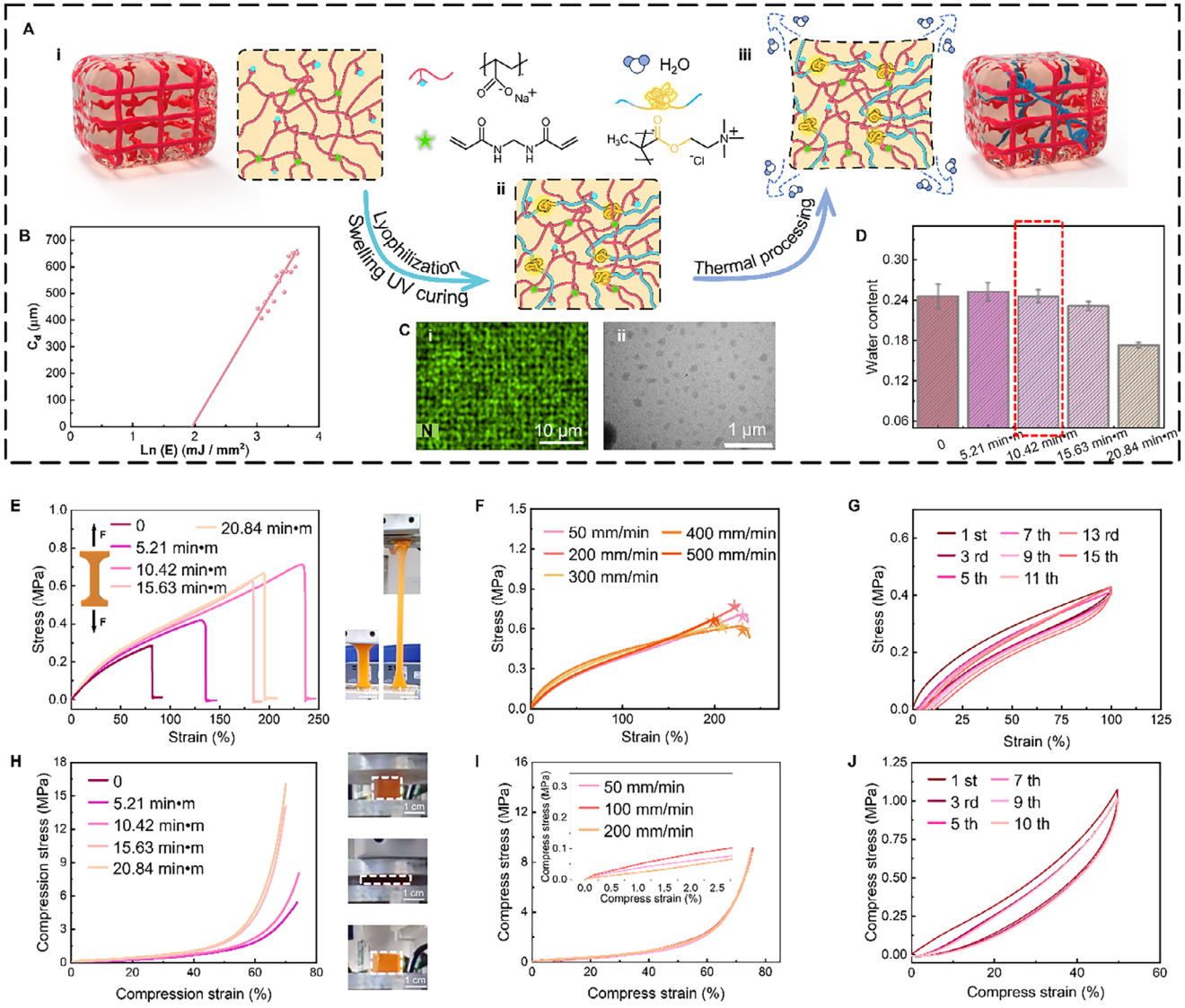

Figure 2. The fabrication and mechanical properties of the DLP-printed hydrogel. A) schematic diagram of two-step post-processing method. B) Jacob's working curves of PAAc inks. C) After the swelling and UV-curing processing, the introduction of a second network was confirmed through the SEM-EDX mapping image of N i), and the AFM phase image ii) for the proof of phase separation inside PMETAC. D) After thermal annealing, the water content inside the hydrogel sample changed. E) True stress–strain curves of the hydrogel samples after different annealing times, and the digital pictures of G-20.42 during stretching. F) True stress–strain curves of G-10.42 at different loading rates. G) Cyclic true stress–strain curves of G-10.42 at a strain of 100% for 11 cycles. H) Compression test of hydrogel samples after a series of annealing times and the digital pictures of G-10.42 during stretching. I) Compression tests of G-10.42 at different loading rates. J) Cyclic compression stress–strain curves of G-10.42 at 50% compression strain.

However, the uniaxial stretchability first improved from 81.79% (G-0) to 237.29% (G-10.42) and then decreased to 184.62% (G-20.84). This behavior resulted from the synergistic effect of network density and the elasticity of hydrophobic clusters. Under applied force, the hydrophobic clusters extended, and when the force was released, the extended chains promptly refolded back into their initial clusters in the water environment, contributing to hyperelasticity.[28] However, too high-density networks can hinder the movement of hydrophobic clusters. Furthermore, G-10.42 showed weak strain-rate dependence and fully recovered from 100% strain to its initial state within seconds, displaying excellent reversibility (Figure 2F,G). The compressibility was also excellent, with weak compression-rate dependence (Figure 2H,I) and superb cyclic performance (Figure 2J).

2.2. Electric and Sensing Performance

The incorporation of PMETAC network substantially improved ionic conductivity through increased free ion concentration, elevating ionic conductivity from 0.09 S m^{-1} (G-PAAc) to 0.15 S m^{-1} (G-5.21) and peaking at 0.16 S m^{-1} (G-10.42). Beyond this point, the high-density double network impeded ion transport, reducing ionic conductivity to 0.1 S m^{-1} (G-20.84) (**Figure** 3A).

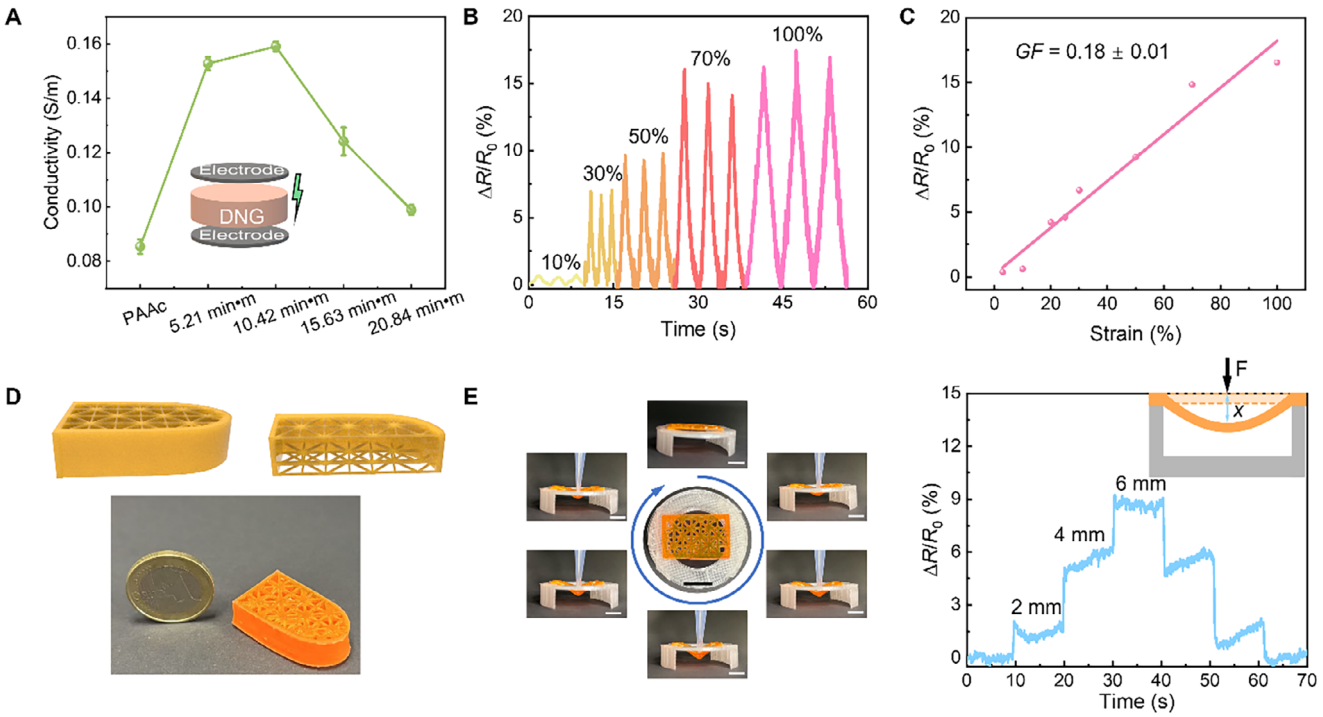

Figure 3. A) Conductivities of double network hydrogel (DNG) samples before and after different annealing times. B) Sensing performance of G-10.42 under series strain. C) Gauge factor of G-10.42 with segmented strain regions. D) Schematic diagram and photo of HBAF. E) State changes of the suspended G-10.42 layer during mechanical loading and unloading and the corresponding relative resistance changes.

G-10.42 demonstrated the ideal combination of stretchability (237.29%) and ionic conductivity (0.16 S m^{-1}), making it the optimal choice for HBAF development. Systematic deformation testing confirmed its reliable sensing performance in the artificial fingertip application. The sensing signals were produced under different strains, testing as the normalized electrical resistance change ($\Delta R/R_0$),

$$\frac{\Delta R}{R_0} = \frac{R - R_0}{R_0} \tag{3}$$

where R refers to the real-time resistance and R_0 means the initial resistance of G-10.42 at the relaxed state. Meanwhile, the tensile strain (ϵ) was calculated as,

$$\epsilon = \frac{(L - L_0)}{(L_0)} \tag{4}$$

where L and L_0 refer to the SDG length at the tensile state and the relaxed state, respectively.

As shown in Figure 3B and G-10.42 exhibited reversible and stable relative resistance changes across a broad strain range (ϵ: 10%–100%). To quantify sensitivity, the gauge factor (GF) was calculated as the ratio of relative resistance change ($\Delta R/R_0$) to applied tensile strain (ϵ). In air, G-10.42 demonstrated a GF of 0.18 ± 0.01 (Figure 3C).

HBAF was designed as shown in Figure 3D. To optimize the suspended structure effectively, HBAF was designed with sensing layers within a porous lattice architecture. The different surface structure in the vertical and lateral surfaces guaranteed that the main deformation occurred on the lateral sensing layers rather than the vertical skeleton (Figure S6, Supporting Information). To simulate the deformation behavior of the sensing layer in HBAF under compression, we tested a suspended G-10.42 film under stepwise pressing (Figure 3E). The sensor reliably tracked each deformation with high precision, maintaining a stable signal platform (Figure 3E; Figure S7, Supporting Information). The sensing response time of 1.67 s (Figure S8, Supporting Information) originates from elastic hysteresis, as the polymeric network requires this time to adapt to deformation. Because the signal here was produced under different strains, testing as the normalized sheet resistance change, the pressing point had no significant influence on the signal strengthening (Figure S9, Supporting Information). These results confirmed that the G-10.42 layer provided accurate, real-time strain monitoring with excellent signal fidelity, making it ideal for dynamic motion detection in HBAF.

2.3. Interface Growth of Adhesive Layer

During the application of HBAF with robotic components, another essential prerequisite is the stable integration between HBAF and robotic elements. Here, a layer of PDA gel was grown under the HBAF. **Figure** 4A shows the mechanism of how the PDA gel layer robustly bonded with HBAF. For this, first, the precursor solution consisting of PDA, acrylamide (AM), and water-soluble photoinitiator TPO-Li was solidified into a PDA gel layer upon patterned UV projection (Figure 4Ai). During AM polymerization, DA was also induced by TPO-Li to further polymerize.

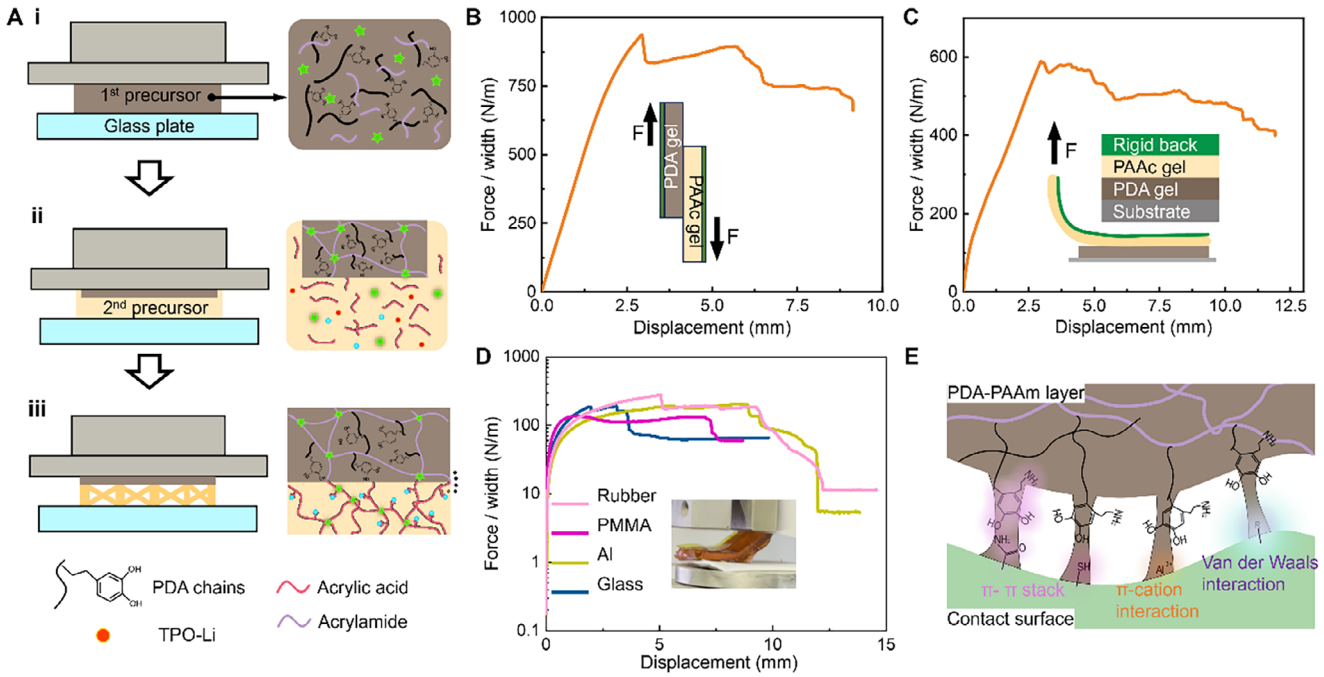

Figure 4. A) Schematic diagram of the process of printing a multi-material hydrogel model. The bonding force between PAAc-PDA hydrogel layers were measured by the parallel B) and vertical C) peeling test. D) Peeling curves of PDA gel layer with various contact surfaces, and E) their adhesion mechanism.

Notably, a small amount of unreacted AM remained in the PDA gel (Figure 4Aii). The PAAc hydrogel was then printed onto the PDA gel layer by projecting a UV pattern into the AAc polymer precursor. At the interface, radicals of the growing PAAc polymer could add unreacted AM monomers to the chain, resulting in an enhanced interfacial contact, or induce a chain transfer with oligomers in the PDA gel domain, resulting in a chemical bonding between the PDA gel layer and PAAc hydrogel layer (Figure 4Aiii; Figure S10, Supporting Information).

To confirm the bonding force between two gel layers, the PDA gel was peeled from the PAAc hydrogel in two different directions: parallel and vertical (Figure S11, Supporting Information). The corresponding peeling forces were 862.76 N m^{-1} (Figure 4B) and 577.59 N m^{-1} (Figure 4C), respectively. The strong bonding force guaranteed the stable sensing performance in the dynamic environment of HBAF. The PDA gel layer demonstrated remarkable adhesive properties to various contact surfaces including rubber, plastic, metal, and glass. We evaluated the adhesive force through a 90° peeling test (Figure S12, Supporting Information). As shown in Figure 4D, the PDA gel layer on the PAAc hydrogel exhibited peeling forces per unit width of 266.78N m^{-1} (rubber), 118.61 N m^{-1} (PMMA), 177.65 N m^{-1} (aluminum), and 122.06 N m^{-1} (glass) on average, which are common hydrophobic substrates used in robotic construction (Figure S13, Supporting Information). The free catechol groups in PDA interacted with amine or thiol groups to form cation-π, π–π interactions, or van der Waals interactions with contact surfaces (Figure 4E).[19] This strong adhesion ensured accurate and stable sensing during practical applications.

2.4. Sensing Performance of HBAF

The touch and pain-sensing mechanism of HBAF (Figure S14, Supporting Information) was then investigated (see **Figure 5**). As shown in Figure 5A, the deformation was further proved by the mechanical simulation. During pressing, deformation of the upper layer primarily drives resistance changed. As displacement increased, the resistance rose (consistent with Figure 3 results), defining this stage as the touch phase. With greater displacement, the first layer contacted the second layer, creating the first short circuit and causing an abrupt resistance drop-defined as the first pain point (first pain point, slight pain), which means the touch was uncomfortable and one should be cautious. When displacement further increased to overlap all three layers, a second short circuit occurred, producing another resistance decrease (second pain point, sharp pain). At this stage, the robotic hand experiences high pain, which is regarded as the dangerous touch and should be avoided. Subsequently, resistance gradually recovered to initial levels when the pressure was drawn back. With this multi-intensity pain perception mechanism, the humanoid robotic hand could mimic the tactile of a human hand and evaluate the safe factor of gripping.

Finally, we mimicked a human finger exploration with pain sensing using the robotic hand (Figures S15 and S16, Supporting Information). As shown in Figure 5B, contact with a flat surface at a small bending angle (70°) produced an abrupt, sharp resistance change, indicating strong pain perception (Figure 5Bi). When the bending angle increased to 75° or 80°, the resistance drop became smaller, corresponding to a reduced pain intensity.

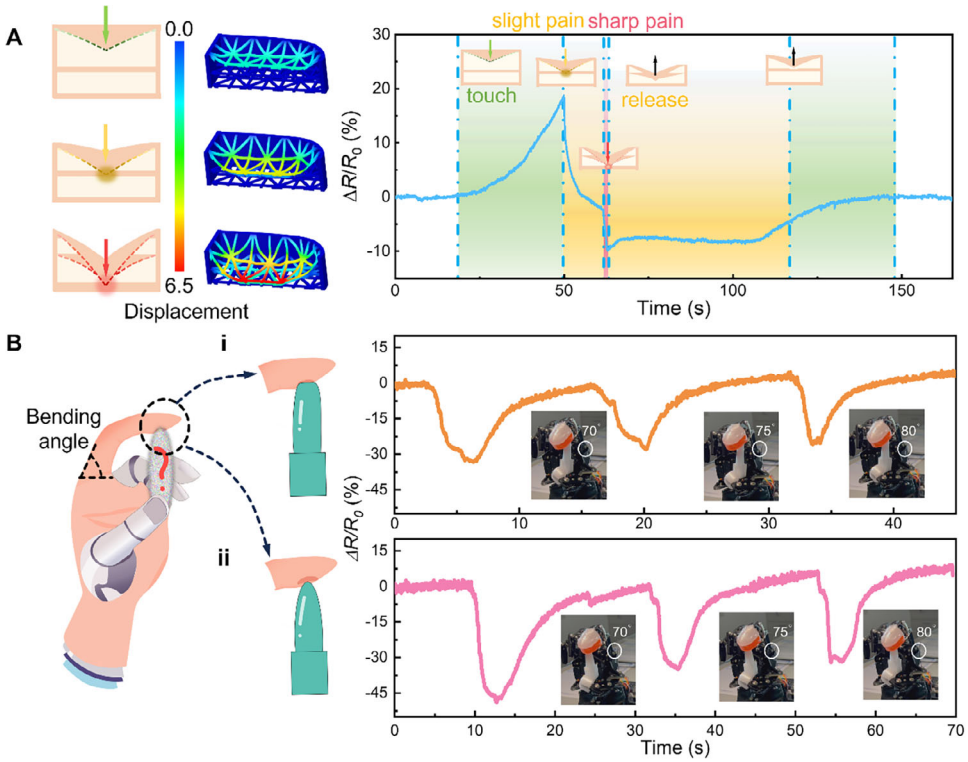

Figure 5. A) The mechanism, corresponding simulation of pain perception of HBAF, and the relative resistance changes during the pressing process. B) The sensing signals when the robotic fingertip contacted with a flat surface i) and sharp tip ii) at different bending angles.

Contact with sharper surfaces (Figure 5Bii) induced significantly deeper resistance drops compared to flat surfaces. Similarly, the relative resistance change (representing pain perception) decreased with increasing bending angle. These results demonstrate that the HBAF-equipped sensor can reliably evaluate contact safety through resistance changes, effectively mimicking the impulse variations observed during mechanical stimulation of human skin.

Moreover, because of the high resolution and programmability of DLP, the pain threshold could be designed through the distance between sensing layers, which shows great potential for a self-protection system with demanded safe factors (SF). For robots requiring enhanced safety protocols - specifically those designed to perceive pain at relatively low thresholds and reach the first pain point more rapidly - the interlayer distance between the upper two protective layers can be reduced compared to systems with lower SF. This design modification accommodates the earlier onset of abrupt current increases associated with pain detection. Two models with different layers setting (Figure S17, Supporting Information) were printed and measured under the pressing of the small pipette tip in a small speed. For easier comparison, only the inner layer distance was regulated, while the height of the two models was the same. As shown in Figure S18 (Supporting Information), the touch phase (green) of Model I was shorter than that of Model II, because the distance between the upper two layers was smaller in Model I. In other words, the lower the slight pain threshold was, the higher the SF was in Model I. At the same time, the second layer was farther distanced from the third layer in Model I, so the slight pain area (yellow) was larger than that in Model II. Since the heights of two models were the same, the sharp pain point came nearly at the same time. The recovery phase was correspondingly different, resulting from the different distance parameters. Model I needed a longer time to recover to the original resistance because the time the sensing layer overlapped was longer. The relative resistance changes were small in these two models because of the small contact area of the pipette tip.

3. Conclusion

A 3D-printed hydrogel-based artificial fingertip (HBAF) sensor was developed to equip robotic fingertips with tactile and pain perception. To enhance the stretchability of the DLP 3D-printed hydrogel and ensure reliable signal generation under pressure, a two-step post-processing method was introduced to incorporate an amphiphilic polymeric network (PMETAC) into the 3D structure without compromising its structural resolution. This modification nearly tripled the hydrogel's stretchability compared to its initial state. Beyond mechanical enhancement, this post-processing strategy offered a versatile platform for integrating additional functionalities, such as self-healing or high conductivity, through alternative functional polymer networks.

Unlike conventional multi-layered sensing systems, the HBAF was fully soft, monolithic, and exhibits high structural stability, enabling seamless adaptation to uneven or curved surfaces. Leveraging multi-interface DLP technology, an adhesive polydopamine (PDA) gel layer was fabricated at the base of the HBAF to facilitate robust integration with rigid robotic substrates. When

mounted on a robotic fingertip, the HBAF successfully discriminated against pain levels based on object sharpness (radius) and finger bending angle. The DLP process enables precise tuning of the HBAF's safety factor through interlayer spacing. Combining with the geometry design, our novel soft sensor - with its programmed modulus and pain perception - can be arrayed on robotic components like artificial hands,[29–32] enabling customizable pain-response systems for clinical and biomedical robotics. However, this soft nature and reliance on precise layer spacing of HBAF make integration with soft robotics challenging, as actuation compromises sensing stability. Hence, the development of more stable structural designs for this purpose is a key focus of ongoing research.

Supporting Information

Supporting Information is available from the Wiley Online Library or from the author.

Acknowledgements

This work was supported by the Helmholtz Association (43.33.11), China Scholarship Council and DAAD Research grant (91865546). A.S., F.H.S. from Jena Center for Soft Matter (JCSM), Friedrich-Schiller-University Jena are grateful for support from the DFG within the SFB 1278 "PolyTarget" (project number 316213987, project B04). The TEM facilities of the Jena Center for Soft Matter (JCSM) were established with a grant from the German Research Council (DFG) and the European Fonds for Regional Development (EFRE). The authors also acknowledge Dr. Martina Plank from the Institute of Functional Interface (IFG) Lahann Lab, KIT, for her help with the SEM; Dipl.-Biol. Peter Krolla from Institute of Functional Interfaces (IFG), KIT, for his help with AFM; Xiaohe Xu, Huan Zhang from Institute for Chemical Technology and Polymer Chemistry (ITCP), KIT, for their help with DLP and the universal-tensile machine; Dr. Erich Müller from the Laboratory for Electron Microscopy (LEM), KIT, for his help with the EDX.

Conflict of Interest

The authors declare no conflict of interest.

Data Availability Statement

The data that support the findings of this study are available in the supplementary material of this article.

Keywords

artificial fingertip, DLP printing, human-robot interaction, pain perception, two-step post-processing

Received: September 5, 2025
Revised: October 2, 2025
Published online:

[1] J. D. Greenspan, R. H. LaMotte, *J. Hand Ther.* **1993**, *6*, 75.
[2] V. G. Macefield, *J. Physiol.* **2022**, *600*, 1539.
[3] H. E. Torebjörk, Å. B. Vallbo, J. L. Ochoa, *Brain* **1987**, *110*, 1509.
[4] I. Birznieks, V. G. Macefield, G. Westling, R. S. Johansson, *J. Neurosci.* **2009**, *29*, 9370.
[5] L. E. Osborn, A. Dragomir, J. L. Betthauser, C. L. Hunt, H. H. Nguyen, R. R. Kaliki, N. V. Thakor, *Sci. Robot.* **2018**, *3*, aat3818.
[6] W. Zhou, Y. Yu, P. Xiao, F. Deng, Y. Zhang, T. Chen, *Adv. Mater.* **2024**, *36*, 2403447.
[7] F. Li, S. Gao, Y. Lu, W. Asghar, J. Cao, C. Hu, H. Yang, Y. Wu, S. Li, J. Shang, M. Liao, Y. Liu, R.-W. Li, *Adv. Sci.* **2021**, *8*, 2004208.
[8] M.d. A. Rahman, S. Walia, S. Naznee, M. Taha, S. Nirantar, F. Rahman, M. Bhaskaran, S. Sriram, *Adv. Intell. Syst.* **2020**, *2*, 2000094.
[9] F. Yu, J. C. Cai, L. Q. Zhu, M. Sheikhi, Y. H. Zeng, W. Guo, Z. Y. Ren, H. Xiao, J. C. Ye, C.-H. Lin, A. B. Wong, T. Wu, *ACS Appl. Mater. Interfaces* **2020**, *12*, 26258.
[10] Y. Sun, Y. Dong, Z. Li, Q. Li, M. Liu, Q. Yuan, B. Li, *Chem. Eng. J.* **2024**, *482*, 148945.
[11] P. Xiao, W. Zhou, Y. Liang, S.-W. Kuo, Q. Yang, T. Chen, *Adv. Funct. Mater.* **2022**, *32*, 2201812.
[12] J. Choi, C. Han, D. Lee, H. Kim, G. Lee, J.-H. Ha, Y. Jeong, J. Ahn, H. Park, H. Han, S. Cho, J. Gu, I. Park, *Sci. Adv.* **2025**, *11*, adv0057.
[13] N. Li, F. Zhan, M. Guo, X. Yuan, X. Chen, Y. Li, G. Zhang, L. Wang, J. Liu, *Adv. Mater.* **2025**, *37*, 2419524.
[14] V. E. Abraira, D. D. Ginty, *Neuron* **2013**, *79*, 618.
[15] R. S. Johansson, A. B. Vallbo, *J. Physiol.* **1979**, *297*, 405.
[16] S. Tajik, C. N. Garcia, S. Gillooley, L. Tayebi, *Regen. Eng. Transl. Med.* **2022**, *9*, 29.
[17] Z. Guo, C. Ma, W. Xie, A. Tang, W. Liu, *Carbohydr. Polym.* **2023**, *315*, 121006.
[18] G. Zhu, Y. Hou, J. Xu, N. Zhao, *Adv. Funct. Mater.* **2021**, *31*, 2007173.
[19] G. Zhu, N. von Coelln, Y. Hou, C. Vazquez-Martel, C. A. Spiegel, P. Tegeder, E. Blasco, *Adv. Mater.* **2024**, *36*, 2401561.
[20] L. Han, L. Yan, K. Wang, L. Fang, H. Zhang, Y. Tang, Y. Ding, L.-T. Weng, J. Xu, J. Weng, Y. Liu, F. Ren, X. Lu, *NPG Asia Mater.* **2017**, *9*, 372.
[21] T. Majima, W. Schnabel, W. Weber, *Makromol. Chem.* **1991**, 2307.
[22] S. Benedikt, J. Wang, M. Markovic, N. Moszner, K. Dietliker, A. Ovsianikov, H. Grützmacher, R. Liska, *J. Polym. Sci. Part Polym. Chem.* **2016**, *54*, 473.
[23] A. A. Pawar, G. Saada, I. Cooperstein, L. Larush, J. A. Jackman, S. R. Tabaei, N.-J. Cho, S. Magdassi, *Sci. Adv.* **2016**, *2*, 1501381.
[24] A. W. Bassett, A. E. Honnig, C. M. Breyta, I. C. Dunn, J. J. La Scala, J. F. I. Stanzione, *ACS Sustain. Chem. Eng.* **2020**, *8*, 5626.
[25] A. Champion, B. Metral, A.-S. Schuller, C. Croutxé-Barghorn, C. Ley, L. Halbardier, X. Allonas, *ChemPhotoChem* **2021**, *5*, 839.
[26] M. Sandmeier, N. Paunović, R. Conti, L. Hofmann, J. Wang, Z. Luo, K. Masania, N. Wu, N. Kleger, F. B. Coulter, A. R. Studart, H. Grützmacher, J.-C. Leroux, Y. Bao, *Macromolecules* **2021**, *54*, 7830.
[27] R. Zhu, D. Zhu, Z. Zheng, X. Wang, *Nat. Commun.* **2024**, *15*, 1344.
[28] L. Chen, Z. Jin, W. Feng, L. Sun, H. Xu, C. Wang, *Science* **2024**, *383*, 1455.
[29] J. Baek, Y. Shan, M. Mylvaganan, Y. Zhang, X. Yang, F. Qin, K. Zhao, H. W. Song, H. Mao, S. Lee, *Adv. Mater.* **2023**, *35*, 2304070.
[30] A. K. Sinha, G. L. Goh, W. Y. Yeong, Y. Cai, *Adv. Mater. Interfaces* **2022**, *9*, 2200621.
[31] A. K. Sinha, G. L. Goh, W. Q. Jaw, G. Chen, L. Pothunuri, W. Y. Yeong, Y. Cai, *Adv. Eng. Mater.* **2025**, *27*, 2401988.
[32] C. Liu, N. Huang, F. Xu, J. Tong, Z. Chen, X. Gui, Y. Fu, C. Lao, *Polymers* **2018**, *10*, 629.